J. Fluid Mech. (2001), *vol.* 442, *pp.* 89–117. Printed in the United Kingdom

Turbulent shear flow over active and passive porous surfaces

By JAVIER JIMÉNEZ[1,2], MARKUS UHLMANN[1], ALFREDO PINELLI[1] AND GENTA KAWAHARA[3]

[1]School of Aeronautics, Universidad Politécnica, 28040 Madrid, Spain

[2]Centre for Turbulence Research, Stanford University, Stanford, CA 94305, USA

[3]Ehime University, Matsuyama 790-8577, Japan

(Received 14 September 2000 and in revised form 21 February 2001)

The behaviour of turbulent shear flow over a mass-neutral permeable wall is studied numerically. The transpiration is assumed to be proportional to the local pressure fluctuations. It is first shown that the friction coefficient increases by up to 40% over passively porous walls, even for relatively small porosities. This is associated with the presence of large spanwise rollers, originating from a linear instability which is related both to the Kelvin–Helmholtz instability of shear layers, and to the neutral inviscid shear waves of the mean turbulent profile. It is shown that the rollers can be forced by patterned active transpiration through the wall, also leading to a large increase in friction when the phase velocity of the forcing resonates with the linear eigenfunctions mentioned above. Phase-lock averaging of the forced solutions is used to further clarify the flow mechanism. This study is motivated by the control of separation in boundary layers.

1. Introduction

Control of wall-bounded turbulent flows is both a technologically rewarding field, and a scientifically interesting problem. Both points of view are complementary. Physical understanding can be expected to lead to better control strategies, and the development and testing of successful control algorithms gives us clues about the physical mechanisms which are active in the flow. In this paper we will concern ourselves with the control of the skin friction in a turbulent channel by means of variable wall transpiration. We will first study the effect of a uniformly permeable wall in which the transpiration velocity is proportional to the local wall pressure fluctuations. This will lead us to the consideration of the linear stability of the flow as a whole, and to the study of channels in which patterned transpiration is applied directly, independently of the pressure. The results of these forced experiments will allow us to study the modifications of the flow in more detail, and will give us hints on the dynamics of wall-bounded flows in general.

Boundary layer control is an old subject which has traditionally been associated with wall manipulation, such as suction and blowing or patterned and compliant walls, but it has been revived in recent years due to the perceived possibility of using micromechanical devices (MEMS, see Löfdahl & Gad-el-Hak 1999) to implement closed loop control mechanisms in which flow variables are locally measured and acted upon (see e.g. Gad el Hak & Blackwelder 1989; Choi, Moin & Kim 1994; Jiménez 1994). Our emphasis in this paper is more classical. Although we will consider

open-loop variable transpiration that can probably only be implemented by MEMS actuators, we will not assume knowledge of the local flow state. The advantages of such an approach in terms of implementation simplicity are obvious and have, for example, been discussed by Schoppa & Hussain (1997).

It might come as a surprise that our stated goal is to increase, rather than to decrease, wall drag. There are of course many cases in which a higher turbulence level is a desirable feature, such as in enhancing mixing and heat transfer, but even in the field of aeronautics, where the desired result is usually to decrease global drag, local drag increase may be beneficial. An obvious example, which was the original motivation for our study, is the use of leading-edge vortex generators and roughness strips to energize the boundary layer and to prevent downstream separation. Drag is increased locally, but decreased globally.

In a different application Carpenter (1996) proposed the use of permeable walls to delay transition. Porosity dissipates energy by moving fluid through viscous pores in the wall, and his idea was that this extra dissipation could be used to damp the growth of the Tollmien–Schlichting waves. Although this would probably increase the global drag of a flat plate, it could be useful in delaying transition across a locally adverse pressure gradient.

Porous walls were shown experimentally to increase skin friction in turbulent boundary layers by Kong & Schetz (1982) and Wilkinson (1983). They also showed that the increase of the turbulent fluctuations was only moderate, and that there were no large changes in the structural properties of turbulence near the wall. Although it was clear that the energy dissipated by the fluid crossing the wall was at the root of the increase in friction, the detailed mechanism remained unclear.

An application of porous surfaces to flow control which is unrelated to the subject of our paper, but which should perhaps be mentioned, is their use to alleviate adverse pressure gradients and flow unsteadiness by allowing large-scale flows inside a wing through an inner plenum chamber. For examples and related references, see the papers by Addington, Schreck & Luttges (1992) and Gillan (1995).

In this paper we will concern ourselves with the effect of porosity, whether active or passive, on the fully turbulent flow in a channel in which the effect of the streamwise pressure gradient has been removed from the transpiration velocity. The details of the numerical technique and of the simulations are discussed first. The effect of passive porous walls on the flow are discussed in § 4, followed by the analysis of the linear stability of the flow in § 5, and of the transient behaviour during switch-on and switch-off of the porosity in § 6. We then present the results of the numerical experiments with patterned forced transpiration, and finally offer a discussion of the results, and conclusions.

2. The numerical experiments

We consider direct numerical simulations of an incompressible plane channel in a box that is doubly periodic in the streamwise, x, and spanwise, z, directions.

Our numerical method is broadly similar to that of Kim, Moin & Moser (1987). The equations are written in terms of the wall-normal vorticity ω_y and of the Laplacian of the wall-normal velocity $\varphi = \nabla^2 v$. The fluid density is assumed to be unity for convenience. The spatial discretization is spectral in (x, z) using Fourier series, but in the wall-normal direction, y, we use B-splines instead of the more usual Chebychev polynomials. The quadratic spacing of the Chebychev collocation points near the walls results otherwise in an unacceptable restriction of the time step whenever, as in

the neighbourhood of porous walls, the wall-normal velocity does not vanish at the boundary.

Our B-spline method is hybrid: the nonlinear terms are evaluated by a collocation scheme, based on fourth-order splines with an explicit finite-difference stencil for the first derivative (Lucas 1974; Houstis, Vavalis & Rice 1988). The remaining terms, including the pressure equation needed for the porous boundary condition, are treated by a Galerkin method, resulting in an overall fourth-order spatial accuracy in y. The time discretization is third-order Runge–Kutta for the nonlinear convective terms, which are computed in physical space using dealiasing in (x, z) according to the $2/3$ rule, and implicit Euler for the viscous terms. Full details of the numerical method are given by Jiménez, Pinelli & Uhlmann (1998).

2.1. *The porous boundary*

The no-slip condition is imposed at both walls. The wall at $y = 2h = 2$ is impermeable, but the one at $y = 0$ is porous, and the fluid crosses it with a wall-normal velocity which is proportional to the pressure *fluctuations*. The boundary condition at $y = 0$ is then

$$u = w = 0, \quad v = -\beta p', \tag{2.1}$$

where u, v, w are streamwise, wall-normal and spanwise velocity components, and $p' = p - G(t)x$ is the instantaneous fluctuation of the wall pressure with respect to the mean pressure gradient, which is continuously adjusted by the code to enforce a constant mass flux. Except for this streamwise gradient, the wall pressure in our simulations is assumed to be periodic in x and in z, and to have zero spatial mean. The use of pressure fluctuations not only ensures an instantaneously zero mass flux through the wall, but also prevents the large-scale streamwise circulation that would otherwise arise, with fluid leaving the channel through the wall at the high-pressure upstream end of the box, and returning to it at the low-pressure downstream end.

This boundary condition mimics the behaviour of a zero-pressure-gradient boundary layer over a Darcy-type porous wall (Batchelor 1967, pp. 223–224) with a constant-pressure plenum chamber underneath. In pipes or channels, or in boundary layers with a downstream pressure gradient, preventing the large-scale circulation along the plenum would require breaking it into narrow spanwise compartments by a series of partitions. Since this might prove difficult in practice, a different control strategy, using active suction and blowing to mimic the effect of porosity, will be discussed in § 7.

The porosity coefficient β in (2.1) has the dimensions of an inverse velocity. The impermeability condition $v = 0$ is recovered for $\beta = 0$, while $\beta \to \infty$ implies zero pressure fluctuations on the wall and an unconstrained wall-normal velocity. A 'perfectly permeable' wall roughly similar to this limit, although not identical, was used in a shearless turbulent flow by Perot & Moin (1995).

Although the pressure does not enter directly in the vorticity formulation of the equations of motion, it is needed for the boundary condition (2.1). We compute it by solving a Poisson equation, as in Kim (1989), with boundary conditions given by the wall-normal momentum balance. Using the no-slip property, and the continuity equation at the porous wall, we obtain

$$\partial_t v + \partial_y p = \nu \varphi, \tag{2.2}$$

where ν is the kinematic viscosity. Eliminating v by means of (2.1) and using a first-order approximation for the temporal derivative, the numerical boundary condition

Case	βU_b	Re_τ^b	Re_τ^t	L_x/h	L_z/h	$N_x \times N_y \times N_z$	Δx^+	Δy^+	Δz^+	tU_b/h
I1	0	181	181	8.17	3.14	$256 \times 192 \times 192$	9.6	0.3–3.8	5.0	125
I2	0.707→0	184		8.17	3.14	$256 \times 192 \times 192$	9.6	0.4–3.9	5.0	–
P1	0.585	198	188	2.69	1.59	$96 \times 160 \times 96$	8.7	0.5–5.0	5.1	250
P2	0.707	214	186	8.17	3.14	$256 \times 192 \times 192$	9.6	0.4–4.5	5.0	145
P3	0→0.707	214	186	8.17	3.14	$256 \times 192 \times 192$	9.6	0.4–4.5	5.0	–
F2	–	192	185	2.69	1.59	$128 \times 160 \times 96$	6.0	0.4–4.9	4.8	160

TABLE 1. Simulation parameters. The porosity coefficient of the lower wall is β, defined in (2.1). The friction Reynolds numbers for the porous and impermeable walls are Re_τ^b and Re_τ^t, respectively. L_x and L_z denote the streamwise and spanwise lengths of the computational domain. N_x, N_y and N_z are the number of collocation points in the three coordinate directions, and Δx^+, Δy^+, Δz^+ are the respective grid spacings in wall units of the porous wall. tU_b/h is the time over which statistics have been accumulated. The transient experiments I2 and P3 are discussed in the text; the parameters given for them are measured at the end of the transient. In the case F2 the forced wall-transpiration condition discussed in § 7 is used at the lower wall.

at the porous wall, $y = 0$, is

$$\partial_y p^{n+1} - \frac{\beta}{\Delta t} p^{n+1} = v\varphi^n - \frac{\beta}{\Delta t} p^n, \tag{2.3}$$

where the superscripts refer to the time step. At the impermeable wall, $y = 2h$,

$$\partial_y p^{n+1} = v\varphi^n. \tag{2.4}$$

These conditions are imposed implicitly to ensure numerical stability.

The velocity is derived from the evolution variables using continuity and the definition of the vorticity. The (0,0) Fourier modes of the two wall-parallel velocity components, which cannot be obtained in this way, are integrated directly from the two mean momentum equations, and it is at this stage that the mean streamwise and spanwise pressure gradients are adjusted at each time step to obtain a constant mass flux.

2.2. *Simulation parameters*

The Reynolds number, based on the channel half-width and on the bulk velocity $U_b = \int_0^{2h} u\,\mathrm{d}y/2h$, is $Re = U_b h/v \approx 2830$ throughout the present work. The results are either normalized with U_b or expressed in wall units based on the friction velocity at each wall, $u_\tau = (v\langle \partial u/\partial y \rangle)^{1/2}$, where $\langle\ \rangle$ represents averaging over wall-parallel planes and over time. The value chosen for Re is comparable to that in the simulations of Kim *et al.* (1987), and leads to $Re_\tau = u_\tau h/v \approx 180$ in channels with two impermeable walls. A summary of the numerical parameters of some representative simulations is given in table 1.

In cases I1 and I2 both walls are impermeable. The former is a reference case used both as an initial condition for some of the porous experiments, and as a test of the accuracy of the code. Its statistics agree well with those of Kim *et al.* (1987). Case I2 is a decay experiment in which the porous wall of case P2 is made suddenly impermeable to test the persistence of the effects of porosity. Conversely, P3 is the sudden start-up of porosity from the impermeable case I1 to P2, and is intended to study the onset of the porosity effects. These two cases are discussed in § 6.

In cases P1 and P2 the lower wall is permeable. The porosity coefficients are chosen to be large enough to have an appreciable effect on the flow, but not so large as to

induce local flow separation, which was a problem with larger values of β. The latter point was not investigated in detail, but it was verified *a posteriori* that instantaneous localized flow reversal occurs only in a negligible fraction of the wall in the cases discussed here.

Finally, the case F2 is given as representative of a series of forced simulations, discussed in § 7, in which porosity was substituted by active suction and blowing.

2.3. *Initial conditions*

An instantaneous flow field from the fully spectral simulation of a channel with two impermeable walls by Jiménez & Pinelli (1999) was used as the initial condition for case I1, which was left to attain statistical equilibrium. Porosity was switched on suddenly from this or from some equivalent equilibrium flow, and the resulting transient was discarded before compiling statistics. The running times quoted in table 1 are counted after statistical equilibrium has been reached for each case.

2.4. *Domain size and grid resolution*

The simulations have been performed in computational domains of two different sizes. The larger box has a streamwise length of between $L_x^+ = 1470$ and 1750 wall units, depending on the flow case. Its spanwise dimension is $L_z^+ = 565$–672. Comparison with previous studies by Kim *et al.* (1987) and by Kim (1989), as well as the *a posteriori* evaluation of the two-point correlations of case I1, indicate that, for impermeable channels at these moderate Reynolds numbers, such a box is large enough not to interfere with even the largest flow scales. We will see later that this is not true with porous walls, and that case P2 contains structures that span most of the computational box, both in the spanwise and in the streamwise directions.

A smaller computational domain was used in case P1. Its dimension corresponds to about three minimal flow units (MFU, Jiménez & Moin 1991) in the spanwise direction ($L_z^+ = 320$), and slightly more than one MFU in the streamwise direction ($L_x^+ = 530$). Data from this case should only be used for qualitative comparisons, especially given the large sizes of the structures mentioned above. On the other hand, a simulation similar to P2, but in the small box of P1, resulted in friction coefficients that differed from those of the larger box by less than 4%. The smaller box was also used for the forced wall transpiration experiments discussed in § 7.

The details of the numerical grids used in our computations are included in table 1. A hyperbolic tangent stretching

$$y = 1 + \tanh(\gamma\xi)/\tanh(\gamma), \quad \xi \in (-1, 1), \tag{2.5}$$

was applied in the wall-normal direction, with the grid being uniform in ξ, and the stretching parameter chosen so that $\Delta y_{max}/\Delta y_{min} \approx 11$. The resolution, expressed in wall units at the bottom wall, was good in all cases.

3. Turbulence statistics

The temporal variation of the instantaneous, (x, z)-plane-averaged, skin friction coefficient $c_f = 2u_\tau^2/U_b^2$, for the simulation P2 is given in figure 1. The most obvious effect of porosity is to substantially increase the mean shear over the porous wall. It is shown in table 2 that, compared to the fully impermeable case I1, the drag increases by 20% in case P1 and by almost 40% in case P2. Since only one of the two walls is made porous in our experiments, a slightly better measure of performance is the ratio between the friction coefficients of the two walls, which is also given in the table.

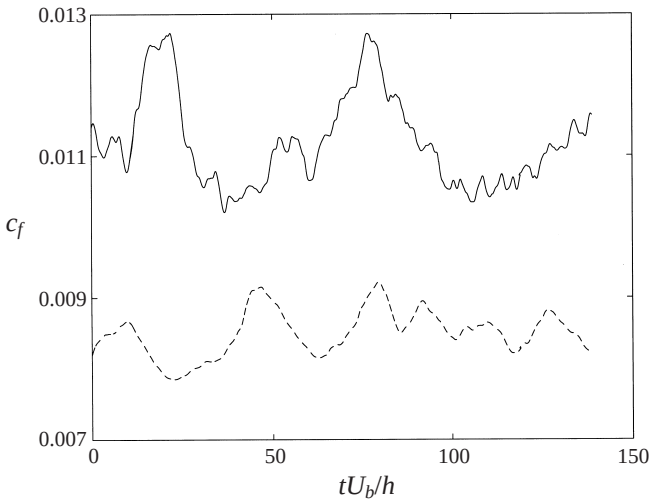

FIGURE 1. Evolution of the plane-averaged wall-friction coefficients in case P2. ————, impermeable wall; ———, porous wall.

Case	v^+_{rms}	c_{fb}/c_{f0}	c_{fb}/c_{ft}	A	y^+_w	$y^+_{\omega_x}$
I1	0	1	1	5.5	42.1	22.9
P1	0.096	1.208	1.106	4.5	28.3	16.8
P2	0.165	1.391	1.325	1.7	35.7	18.9
W5	0.130	1.444		2.8		
CH	−0.125	0.765		8.0		

TABLE 2. Characteristics of porous walls. c_{fb}/c_{f0} is the change of the friction coefficient on the bottom wall with respect to that of the reference case I1. c_{fb}/c_{ft} is the ratio between the friction coefficients of the porous and impermeable walls. A is the additive constant of the logarithmic velocity profile, and v^+_{rms} is the r.m.s. transpiration velocity at the wall. The minus sign in case CH refers to it being an opposition control. y^+_w and $y^+_{\omega_x}$ are the locations of the peaks of the spanwise velocity and of the streamwise vorticity fluctuation profiles, and are discussed in the text. W5 is a 'partially permeable' pipe from Wagner & Friedrich (1998), with $u_\tau R/\nu = 180$, $\alpha = 0.975$ and $\Delta r^+ = 0.2$, as defined in (3.1). Case CH is an active control case in a channel, with $\alpha = -1$, $\Delta y^+ = 5$, from Choi *et al.* (1994).

Table 2 also includes values from two related numerical experiments. Wagner & Friedrich (1998) performed simulations of turbulent pipes with 'permeable', no-slip walls, at Reynolds numbers similar to ours. Their boundary condition for the radial velocity at the wall, $r = R$, is

$$ru_r|_{r=R} = \alpha\, ru_r|_{r=R-\Delta r}. \tag{3.1}$$

It will be seen when we deal in § 5 with the stability of the flow that this condition is linearly equivalent to porosity, at least when viscous effects are neglected. A similar condition was used in the active control experiments of Choi *et al.* (1994), who measured the wall-normal velocity on a plane at some distance from the wall, and applied at the wall a transpiration proportional to it. Since their purpose was to decrease, rather than to increase drag, they chose $\alpha < 0$. We have included in table 2 a 'partially permeable' case from Wagner & Friedrich (1998), and another from Choi

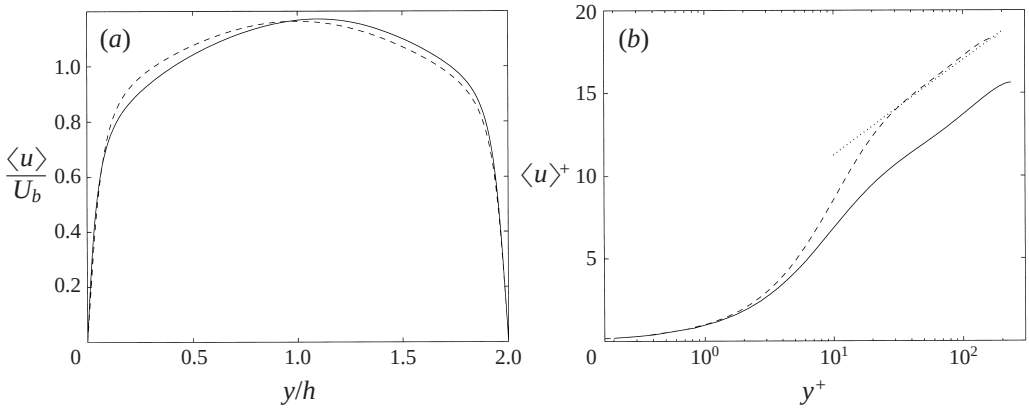

FIGURE 2. Mean velocity profiles. ————, impermeable channel I1; ———, porous case P2. (*a*) Outer scaling; (*b*) wall scaling near the porous wall. The dotted line is $\langle U \rangle^+ = 2.5 \log y^+ + 5.5$.

et al. (1994), with roughly the same normal intensities at the wall. They result in comparable changes in the friction coefficients, although one is positive and the other one negative, and both are of the same order of magnitude as the result of our case P2. The table approximately supports a monotonic change of the increment of the skin friction with the transpiration intensity, and suggests that the effect on the turbulence structure of transpiration patterns generated in very different ways might be similar, at least at moderate intensities. We will see later that this is not strictly true in the present case.

Profiles of mean streamwise velocity $\langle u \rangle$ are shown in figure 2. Since the two walls of the porous channel are different, its velocity profile is asymmetric, biased towards the upper (impermeable) wall. The semi-logarithmic representation shows that the logarithmic behaviour of the velocity above $y^+ = 30$ is preserved with the usual slope $\kappa^{-1} = 2.5$. The value of the intercept of the logarithmic law decreases for the porous wall, as a consequence of the increase of the friction coefficient.

It is interesting to estimate how much of the energy loss implied by the increase in wall friction is due to increased dissipation within the flow, and how much is being directly absorbed at the wall by the porosity condition. The time-averaged equation for the kinetic energy K can be put in the form

$$\langle Gu \rangle + \partial_y \phi = -\langle \varepsilon \rangle, \tag{3.2}$$

where $\varepsilon = \nu |\boldsymbol{\nabla u}|^2$ is the viscous energy dissipation rate and $\phi = \langle vK + vp' - \nu \partial_y K \rangle$ is the wall-normal energy flux. Integrating (3.2) over y, computing the pressure gradient G from the streamwise balance of forces, and using the porosity condition to eliminate the pressure fluctuations, we obtain

$$(\tau_b + \tau_t) U_b = \int_0^{2h} \langle \varepsilon \rangle \, \mathrm{d}y - \langle v^3/2 - v^2/\beta \rangle \, |_{y=0}, \tag{3.3}$$

where τ_b and τ_t are respectively the wall stresses at the bottom and top walls. The second term on the right-hand side of the equation is the energy flux through the wall due to porosity. We can use (3.3) to estimate the increase in wall friction due to this flux,

$$\frac{\Delta \tau}{\tau} = \frac{\Delta c_f}{c_f} = \frac{v_{rms}^{+2}}{\beta U_b} - \frac{u_\tau}{2U_b} \langle v^3 \rangle^+ |_{y=0}. \tag{3.4}$$

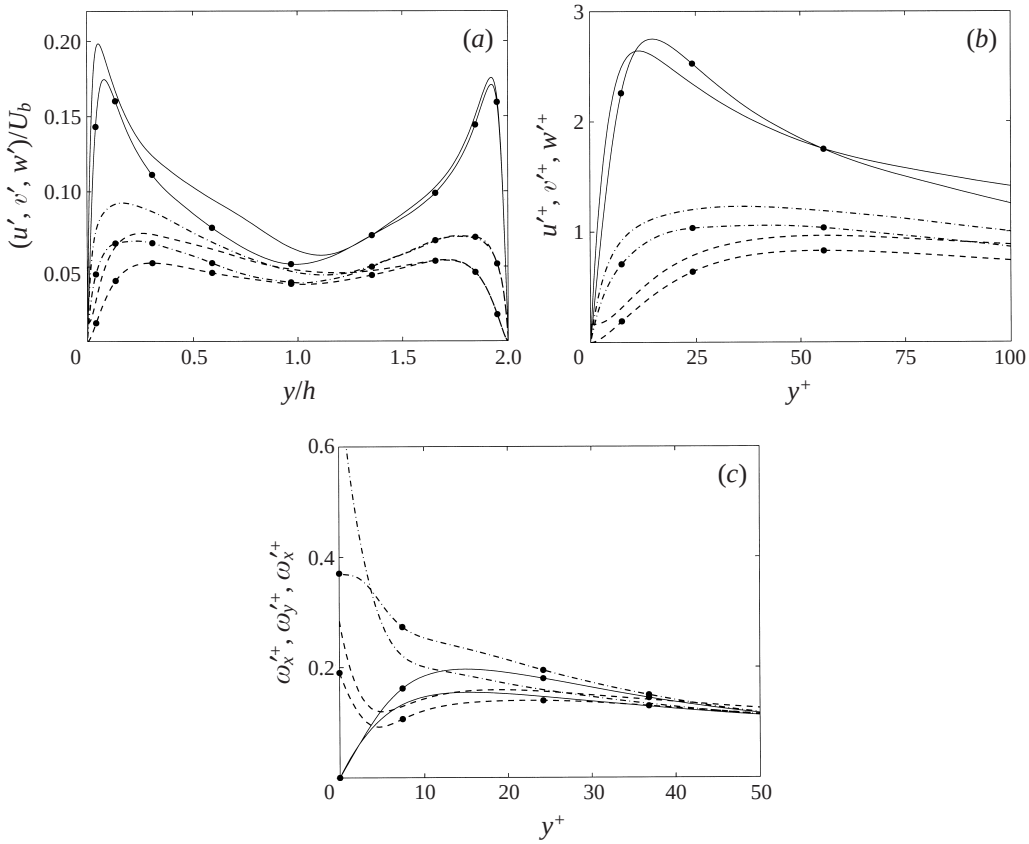

FIGURE 3. Root-mean-square fluctuation intensities for the impermeable case I1 (lines with symbols) and for the porous one P2. (*a*) Velocities. ———, u'; – – – –, v'; —·—, w'. Outer scaling. (*b*) Velocities in wall scaling near the porous wall. (*c*) Vorticities. – – – –, ω_x'; ———, ω_y'; —·—, ω_z'.

The r.m.s. transpiration velocity $v_{rms}^+ = \langle v^2 \rangle^{1/2}$ is given in table 2. Using for example case P2, where $v_{rms}^+ \approx 0.16$ and $\beta U_b \approx 0.7$, the pressure term on the right-hand side of (3.4) is approximately 0.04, while the cubic term is at most of order $v_{rms}^{+3} c_f^{1/2} \approx 10^{-4}$. The pressure term is dominant, but it only explains about 10% of the observed increase in wall friction, which must therefore be due to changes within the flow that increase the bulk viscous dissipation.

3.1. *Fluctuations*

We define in the usual way the fluctuations with respect to the plane average as

$$u = \langle u \rangle(y) + u'. \tag{3.5}$$

It will later be convenient to use spanwise-averaged fluctuations,

$$\bar{u}(x, y, t) = \langle u \rangle_z - \langle u \rangle, \tag{3.6}$$

where the subscripts of $\langle\ \rangle$ denote the variables over which the averaging is done. We reserve $\langle\ \rangle$, without subscripts, for the regular plane averaging over x, z and t. The time average of $\bar{u}$, usually with respect to some moving frame of reference, and the

corresponding triple decomposition of the fluctuations will be denoted by

$$\tilde{u}(x - U_c t, y) = \langle \bar{u} \rangle_t, \quad u = \langle u \rangle + \tilde{u} + u''. \tag{3.7}$$

The advection velocity U_c of the axes will always be clear from the context.

The intensities of the three velocity fluctuations are shown in figures 3(*a*) and 3(*b*). Porosity enhances the three velocity components throughout the lower half of the channel, at least when normalized with the bulk velocity U_b. This effect is strongest for the two transverse components, and less marked for the streamwise one. When the intensities are normalized with the local friction velocity, the increase in the streamwise intensity disappears, but the transverse components are still enhanced. The locations of the peaks of all the fluctuation profiles move closer to the wall. The other half of the channel, especially above $y = 1.5h$, is relatively unaffected by the porosity.

The intensities of the vorticity fluctuations are given in figure 3(*c*). The r.m.s. value of the streamwise component ω_x' is enhanced near the porous wall, and the location of its second maximum is several wall units closer to the wall in the porous case than in the regular channel. This behaviour is consistent with similar effects observed in the control experiments of Choi *et al.* (1994), and in a series of related experiments by Jiménez (1994) in which the spanwise velocity was actively controlled, instead of v. In all of those cases, controls that increase the drag tend to move the fluctuation peaks towards the wall and to strengthen the transverse fluctuations, and vice versa. The strength of the streamwise velocity fluctuations is usually relatively unaffected.

This behaviour was interpreted by Jiménez (1994) as meaning that the main reason for the increase of the wall friction is that the quasi-streamwise vortices move closer to the wall. The maximum of the intensity of ω_x' is commonly associated with the wall-normal location of the quasi-streamwise vortices (Kim *et al.* 1987), and so are the transverse velocity components. The streamwise velocity fluctuations, on the other hand, correspond to the streaks and are not directly connected with the vortices. It was found by Jiménez (1994) that the shift of the peak of the spanwise velocity fluctuations was a good predictor of the skin friction, and a rough model was presented which postdicted this dependence on physical grounds. It is tempting to apply the same criterion here. The location of the spanwise velocity and streamwise vorticity peaks for the two porous experiments are given in table 2. Both are closer to the wall than in the impermeable case, but the shift is smaller than in the experiments cited above, and it is not monotonic with the change in c_f. The reason for the latter is not clear, but we have already noted the dangers of comparing flows with different computational boxes.

Other things are also different here from the case of active control. The peak of ω_y^+ is substantially reduced above the porous wall which, since the main contribution to this vorticity component near the wall is $\partial u/\partial z$ (Jiménez & Pinelli 1999), implies that the streaks are being weakened. Since they are known to be generated by the streamwise vortices, which are strengthened, this suggests that a new mechanism is present in this case.

The fluctuations of the spanwise vorticity fluctuations increase a lot near the porous wall, reaching in P2 nearly twice their usual value. We have verified that this represents fluctuations of the skin friction, rather than a direct contribution of the transpiration through $\partial v/\partial x$. That the fluctuations of the vorticity increase more than its mean also suggests that the mechanism for drag increase is in this case more complex than a simple strengthening of the wall-turbulence cycle.

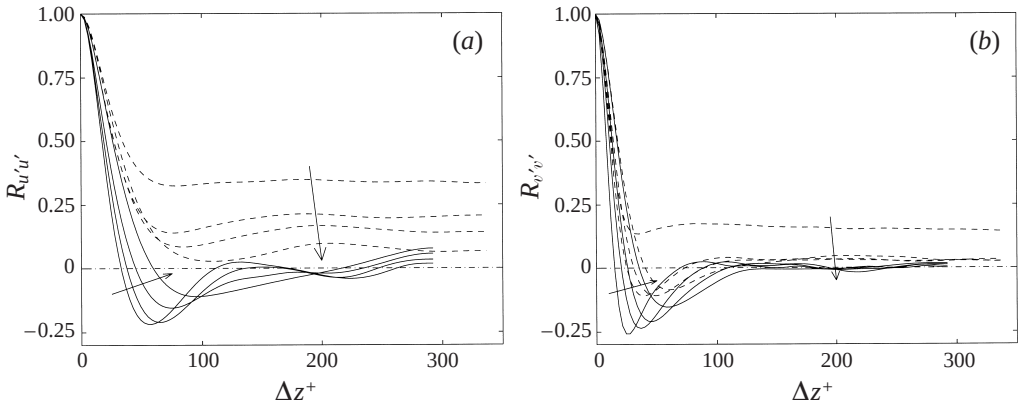

FIGURE 4. Two-point spanwise autocorrelations in the porous channel P2. (*a*) Streamwise velocity; (*b*) wall-normal velocity: ———, impermeable wall; – – – –, porous wall. Lines are shown at $y^+ = 5$, 17, 30, 50, in wall units local to each wall, increasing along the arrows.

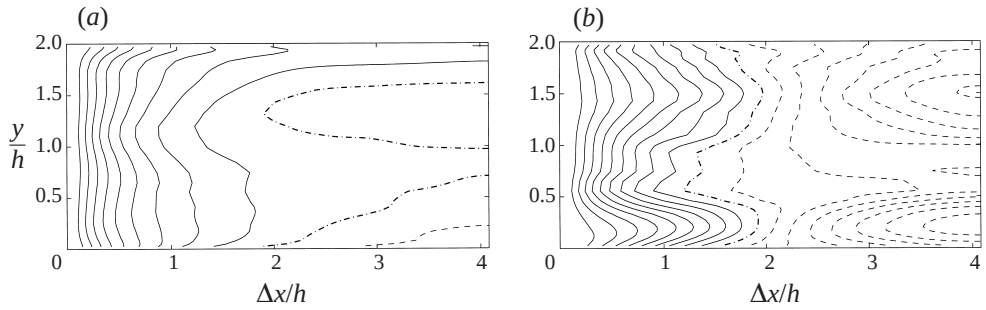

FIGURE 5. Two-point autocorrelations across the channel as a function of the streamwise separation. Case P2. (*a*) $R_{u'u'}$. (*b*) $R_{\tilde{u}\tilde{u}}$. The spacing of the contour lines is 0.1; ———, positive; – – – –, negative; —·—, zero.

4. Structure

Figure 4 shows autocorrelation functions of the streamwise and wall-normal velocity fluctuations near both walls of the porous channel, as a function of the spanwise separation. A full set of correlation functions for the three velocity components and for the pressure can be found in Jiménez *et al.* (1998). In a regular channel, $R_{u'u'}(\Delta z)$ first becomes negative and eventually falls to zero beyond $\Delta z^+ \approx 100$ (Kim *et al.* 1987), and the same behaviour is found here for the impermeable wall. Near the porous wall, however, the correlation does not decay and, especially very close to the wall, reaches a plateau which implies spanwise coherence across the full box. The same is true for $R_{v'v'}$, although only very close to wall. The $R_{p'p'}$ correlations, not shown here, show the same effect, but not $R_{w'w'}$.

The behaviour of the streamwise correlation is more complicated. In a regular channel it decays slower than the spanwise one, because the velocity streaks are elongated in the streamwise direction. Figure 5(*a*) is a contour plot of the streamwise correlation $R_{u'u'}(\Delta x)$ as a function of the wall-normal coordinate y, and should not be confused with a two-dimensional correlation.

The top wall in this figure is essentially similar to those of regular channels at moderate Reynolds numbers. The correlation decays slowly without changing sign,

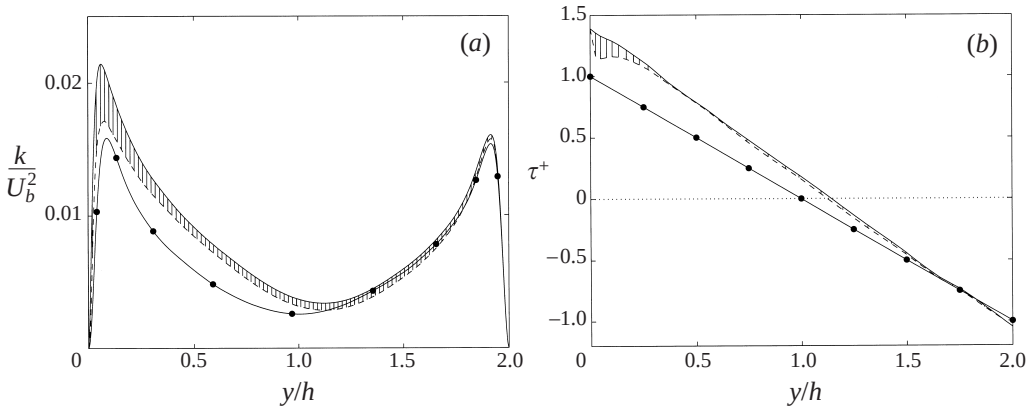

FIGURE 6. Influence of the spanwise-coherent fluctuations in the porous case P2. (*a*) Kinetic energy, $k = \langle u^2 + v^2 + w^2 \rangle / 2$, normalized in outer units: ———, from the total fluctuations u'; – – – –, from the three-dimensional fluctuations, u''. (*b*) Shear stress: ———, total stress, including viscous terms and $-\langle u'v' \rangle$, normalized in wall units of the impermeable channel; – – – –, the same quantity computed from the three-dimensional fluctuations $-\langle u''v'' \rangle$. The hatched area represents in both plots the stresses due to the two-dimensional fluctuations, $\bar{u}$, and the lines with symbols correspond to the impermeable case I1.

with a characteristic length scale of 500–700 wall units. The porous wall is different. The correlation is shorter, and becomes slightly negative at long distances, implying the presence of a weakly coherent structure with a wavelength of the order of the box length.

The behaviour of the spanwise correlations suggests that this structure is also coherent spanwise, and that it should be described well by the spanwise-averaged quantities introduced in (3.6). The streamwise correlation of $\bar{u}$ is given in figure 5(*b*). The reason for the shorter correlations of the full velocity fluctuations near the porous wall is now clear. There is strong spanwise-coherent structure near that wall, whose streamwise wavelength fills the computational box, and which is organized enough for its correlation to be approximately -0.7 at the end of the domain. This structure is reflected, although more weakly, in the upper half of the channel, but it is overwhelmed near the upper wall by the streamwise coherence of the streaks. Although not shown, the correlations of the pressure show a similar effect, extending across the whole channel. Those of the wall-normal velocity are only coherent very near the bottom wall, in agreement with figure 4(*b*), and those of the spanwise velocity show little difference from the regular channel. Details can be found in Jiménez *et al.* (1998).

The two-dimensional structures suggested by these correlations contribute substantially to the turbulent stresses in the neighbourhood of the porous wall. Figure 6(*a*) compares the total fluctuation energy for the porous and for the impermeable channels. The fluctuations are stronger near the porous wall, and it is clear from the figure that a substantial part of the increase is due to the spanwise-coherent component, whose contribution is represented by the hatched area. Note however that, outside the immediate neighbourhood of the wall, most of the change in the energy cannot be explained in this way, implying that, even if the two-dimensional component may explain the modifications of the near-wall layer, it also acts as a trigger of more general changes in the core flow.

The same conclusion can be drawn from figure 6(*b*), which displays total shear

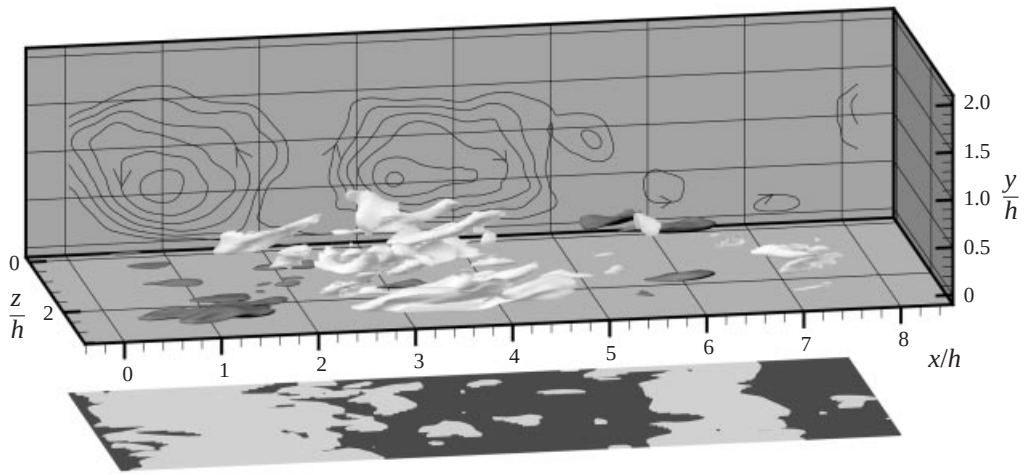

FIGURE 7. Instantaneous isosurfaces of streamwise velocity fluctuations of case P2 with $u'^{+} = \pm 4.5$. Negative values have lighter colour. The streamlines in the back of the box are from the two-dimensional field $(\bar{u}, \bar{v})$. The (x, z) surface underneath indicates regions of local blowing (dark shading) and suction (light shading).

stresses. There is a sizeable contribution near the wall from the two-dimensional Reynolds stress $-\langle \bar{u}\bar{v} \rangle$ but, further into the flow, most of the increase in the friction coefficient of the porous wall is due to changes in the three-dimensional fluctuations.

The visualization in figure 7 clearly shows the approximately two-dimensional organization of the flow. The streamlines of the spanwise-averaged flow are shown on the back plane of the figure, and take the form of large spanwise rollers. The distribution of the transpiration in the porous wall is shown at the bottom of the visualization, displaced from the actual position of the wall for clarity. Although there is nothing intrinsically two-dimensional in the porosity condition (2.1), the transpiration organizes itself into roughly spanwise bands, which are reflected in the interior of the flow by local strengthening of the streamwise velocity streaks. Although we will see below that there is indeed some modulation of the streaks, most of the effect seen in the figure is an artifact of the visualization. The isosurfaces of u' include the streamwise variation of the two-dimensional velocity $\bar{u}$ and, wherever the transpiration is predominantly into the wall, the mean velocity near the wall increases and the low-velocity streaks appear to weaken. The opposite is true in regions of local blowing.

The latter effect is important in explaining the change in the friction coefficient at the porous wall, since suction increases locally the velocity gradient near the wall, and therefore the local skin friction. This is seen in figure 7 from the distribution of the high-velocity isosurfaces, which are plotted in a darker colour. They are found predominantly near the wall, where they mark the location of high skin friction, and tend to cluster in the bands where suction is dominant. The mean velocity gradient decreases in the zones of mean injection, and cancels in part this effect, but it was argued by Orlandi & Jiménez (1994) that, whenever there is a zero-mean wall-normal velocity near the wall, the overall effect is to increase skin friction.

Note that the two rolls do not fill the computational box, suggesting that the preferred wavelength is $\lambda_x/h \approx 5$, somewhat shorter than the box. This seems to disagree with figure 5(b), in which the minimum of the correlation is very close to one half of the box length, but is representative of the instantaneous snapshots of the

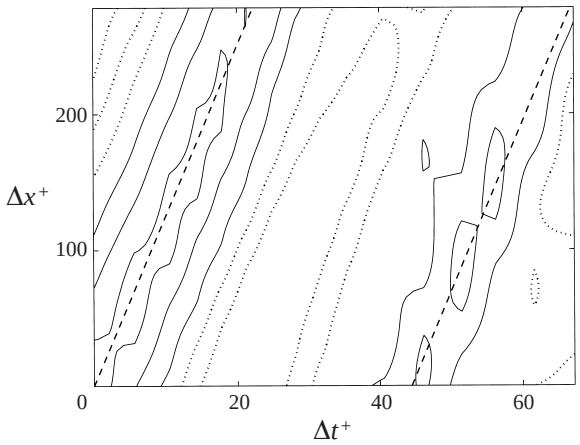

FIGURE 8. Space–time correlation function of the spanwise-averaged fluctuations $\bar{u}$, for the porous case P1. Contours are $R_{\bar{u}\bar{u}} = -0.7(0.1)0.8$, and the dotted contours are negative. The dashed line corresponds to an advection velocity $U_c^+ = 12.5$, based on the friction velocity of the bottom wall.

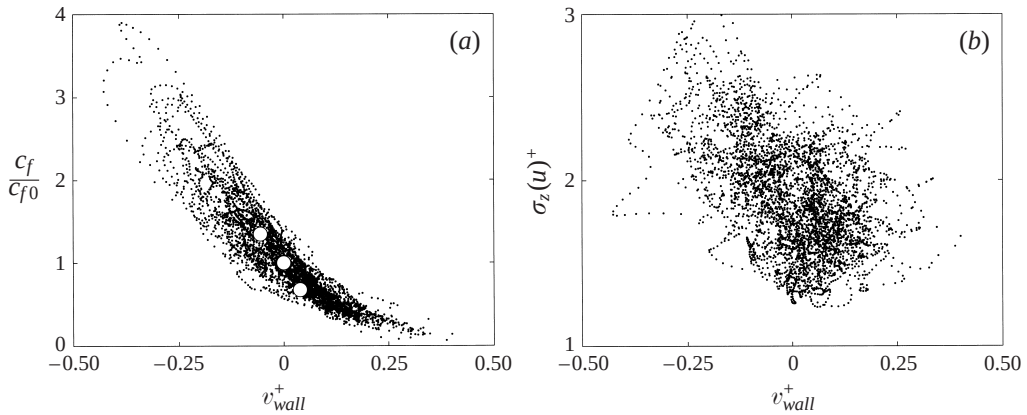

FIGURE 9. (*a*) Scatter plot of the instantaneous spanwise-averaged transpiration velocity at the lower wall, $\bar{v}(x,0)$, compared with the local spanwise-averaged friction coefficient $\langle c_f \rangle_z$. The circles are steady transpiration calculations by Sumitani & Kasagi (1995). (*b*) Scatter plot of $\bar{v}(x-\Delta x,0)$ against the magnitude of the spanwise variation of the streamwise velocity, defined in (4.2). $\Delta x = 1.12$. Both plots are compiled over 17 well-spaced fields of case P2. The intensity in (*b*) has been averaged over $y^+ = 20$–30.

flow. While statistical averages are generally to be preferred to instantaneous views, the two are not necessarily contradictory. It is easy to check, for example, that the autocorrelation function of

$$u = [\sin(x) + \sin(x/2)]^2, \tag{4.1}$$

which is similar to the velocity in figure 7 in that it is formed by a train of double pulses separated by longer gaps, has a minimum at $\Delta x = 2\pi$, which is one half of the distance between the groups of pulses, instead of at some value corresponding to the distance between neighbouring peaks. This is because the statistics average between the distance of each pulse to its leading and to its trailing neighbour.

The two-dimensional rollers advect downstream with a velocity $U_c^+ \approx 12$, as can be seen in the space–time correlation of the longitudinal spanwise-averaged velocity

in figure 8. This advection velocity is approximately the same one measured for the energy-containing structures in the wall layer by most investigators (Kim & Hussain 1993; Jiménez & Pinelli 1999).

The association of the local suction with the increased skin friction is made explicit in figure 9(*a*), which compares the local spanwise-averaged transpiration velocity with the spanwise-averaged skin friction. Both are well correlated, and it is clear that suction increases friction more than blowing decreases it. It is interesting that the observed correlation agrees well, for weak blowing and suction, with the results of Sumitani & Kasagi (1995) for steady uniform transpiration, suggesting that the wavelength of the rollers is long enough for the near-wall effect of transpiration to be close to equilibrium. In figure 9(*b*) we plot the transpiration velocity against a measure of the local strength of the velocity fluctuations, defined by

$$\sigma_z(u)^2 = \langle u^2 \rangle_z - \langle u \rangle_z^2. \tag{4.2}$$

This quantity depends on x, t and y, and is plotted against the transpiration velocity at some distance, $x - \Delta x$, upstream. The offset is chosen to maximize the correlation of both quantities, and the optimum turns out to be $\Delta x/h \approx 1.2$. This value is not any obvious fraction of the length of the box, $L_x/h \approx 8$, but it is close to one half of the distance between the two neighbouring rolls in figure 7. This agrees with the location of the apparent enhancement of the turbulent activity in that figure, and is consistent with the intuitive notion that the space between the two rolls acts as an 'ejection' in promoting the local instability of the flow. Note that $\sigma_z(u)$ does not contain contributions from the modulation of the spanwise-averaged velocity, and is therefore free from the ambiguities mentioned above in relation with figure 7. This association of stronger turbulent fluctuations with the large-scale ejections created by the rollers will be found again in the forcing experiments discussed in § 7 (figure 17*b*).

A last experiment should be briefly mentioned. To check that the rolls were indeed responsible for the increase in skin friction, a numerical simulation was carried out in which the porosity condition (2.1) was applied only to those Fourier components whose streamwise wavenumber was larger than $k_x h = 7$. This prevented the formation of coherent structures with streamwise wavelengths longer than approximately h, but did not inhibit transpiration, which only decreased slightly. The result was that the rolls did not form, and that the skin friction of the porous wall was essentially unchanged from its impermeable value.

5. Linear stability

The spontaneous formation of the large spanwise rollers suggests that they originate from a linear instability of the mean flow, even if the velocity profile of a turbulent channel with impermeable walls was shown by Reynolds & Tiedermann (1967) to be stable. As in that work, we will analyse the stability of the porous case using a linear perturbation of the mean profile, substituting the constant molecular viscosity by the variable isotropic eddy viscosity,

$$\nu_t = u_\tau^2 \frac{1 - y/h}{\partial_y \langle u \rangle}, \tag{5.1}$$

needed to maintain the mean velocity profile. Note that this definition includes the molecular viscosity. Assume perturbation velocities of the form

$$v' = \hat{v}(y) \exp \mathrm{i}[\alpha_1 (x - ct) + \alpha_3 z], \tag{5.2}$$

where the wavenumbers $\alpha_1 > 0$ and α_3 are real, and the phase velocity c is possibly complex. The linearized equation takes the form

$$[\langle u\rangle - c](\partial_{yy} - \bar{\alpha}^2)\,\hat{v} - \langle u\rangle_{yy}\hat{v} + \mathrm{i}\alpha_1^{-1}(\partial_{yy} - \bar{\alpha}^2)[v_t(\partial_{yy} - \bar{\alpha}^2)\,\hat{v}] = -\mathrm{i}\alpha_1 v_{t,yy}\hat{v}, \tag{5.3}$$

where $\bar{\alpha}^2 = \alpha_1^2 + \alpha_3^2$, and the subindices of the mean velocity and eddy viscosity denote derivatives with respect to y. The left-hand side is the standard Orr–Sommerfeld equation, while the extra term on the right-hand side originates from the variation of the eddy viscosity. The impermeability and no-slip boundary conditions take their usual form

$$\hat{v}(2h) = \partial_y\hat{v}(2h) = \partial_y\hat{v}(0) = 0. \tag{5.4}$$

The porosity condition (2.1) holds at the lower wall, with the pressure given by

$$\bar{\alpha}^2\hat{p} = \partial_y[v_t(\partial_{yy} - \bar{\alpha}^2)\hat{v}] + \mathrm{i}\alpha_1\,[\langle u\rangle_y\hat{v} + (c - \langle u\rangle)\partial_y\hat{v}]. \tag{5.5}$$

Note that, except for the viscous terms, this boundary condition is a linear combination of $\hat{v}$ and $\hat{v}_y$, and is therefore essentially equivalent to the 'offset' controls discussed in (3.1).

Except for the right-hand side of (5.3), Squire's transformation (Drazin & Reid 1981, p. 129) reduces the problem to a two-dimensional one with $\alpha_3 = 0$, and a modified viscosity and porosity

$$\hat{\nu}_t = \bar{\alpha}\nu_t/\alpha_1, \quad \hat{\beta} = \alpha_1\beta/\bar{\alpha}. \tag{5.6}$$

Oblique waves therefore behave as if they had higher viscosities and lower porosities than two-dimensional ones with the same $\bar{\alpha}$. Since we will see below that both effects are stabilizing, we will assume from now on that $\alpha_3 = 0$. The right-hand side of (5.3) does not transform correctly under (5.6), but it can be checked numerically that its effect is small and does not modify the previous conclusion.

The possible instability modes obtained in this way generate Reynolds stresses which modify the mean flow and the friction coefficient. Consider a plane channel. If we assume that v' is the real part of (5.2), we obtain

$$\langle u'v'\rangle = 2\,\mathrm{Re}\,(\hat{u}\hat{v}^*) = -2\alpha_1^{-1}\,\mathrm{Im}\,(\hat{v}^*\partial_y\hat{v}), \tag{5.7}$$

where the asterisk stands for complex conjugation, Re( ) and Im( ) are the real and imaginary parts, and the second part of the equation derives from continuity. Note that the approximation (5.7) is consistent even if the stress is a quadratic quantity. This is because, if we consider expansions of the form $v = v_0 + \epsilon v_1 + \epsilon^2 v_2 + \ldots$ for some small amplitude parameter ϵ, the leading contributions to the Reynolds stress are $\langle u_1 v_1\rangle$, $\langle u_0 v_2\rangle$ and $\langle u_2 v_0\rangle$. The zeroth-order terms are constant for a given y, and can be taken out of the averaging brackets. The last two contributions then vanish because continuity ensures that $\langle v_n\rangle = 0$ to all orders. The first one is (5.7).

We can integrate the momentum equation to obtain

$$\nu_t\partial_y\langle u\rangle = \tau_b - \frac{\tau_b + \tau_t}{2}\frac{y}{h} + \langle u'v'\rangle, \tag{5.8}$$

where τ_b and τ_t are the shear stresses at the top and bottom walls. Integrating this equation again gives the velocity profile, and the condition $\langle u\rangle(2h) = 0$ results in a relation between the two wall stresses. Integrating once more gives the bulk velocity. Defining it, for example, to be constant gives another relation, and allows us to compute the change in the friction coefficients. The result for an initially symmetric

channel whose wall stress is τ_0 is

$$\left.\begin{aligned}\frac{\tau_t-\tau_b}{2}&=F_3(2h)/F_1(2h),\\ \frac{\tau_t+\tau_t}{2}&=\tau_0+\frac{G_3-G_1F_3(2h)/F_1(2h)}{G_2},\end{aligned}\right\} \tag{5.9}$$

where

$$F_1(y)=\int_0^y \nu_t^{-1}\mathrm{d}y,\quad F_2(y)=\int_0^y \nu_t^{-1}(1-y/h)\,\mathrm{d}y,\quad F_3(y)=\int_0^y \nu_t^{-1}\langle u'v'\rangle\mathrm{d}y, \tag{5.10}$$

and $G_n=\langle F_n\rangle_y$. There are several strong assumptions in the derivation of this formula, starting with the eddy viscosity approximation itself, but especially the implication that ν_t does not change as a result of the development of the instability. Even mild modifications, such as assuming that ν_t scales with the new u_τ, lead to corrections which are of the same order as those included in (5.8). Numerical experiments, however, as well as the quantitative comparisons in § 7, suggest that the increments of the skin friction predicted by (5.9) can at least be used to compare different control strategies.

5.1. *Inviscid modes*

The origin of the porous instability can most easily be understood from the simplified inviscid analysis of a piecewise-linear profile over a single wall,

$$\begin{aligned}\langle u\rangle &= Uy/h, \quad y<h,\\ &= U, \quad y\geqslant h.\end{aligned} \tag{5.11}$$

In that case (5.3) reduces to a second-order equation, and the only boundary conditions are the porosity relation at the wall, and $\hat{v}\to 0$ as $y\to\infty$. The solution is continuous everywhere and can be expressed as a combination of exponentials $\exp(\pm\alpha_1 y)$. There are two eigenvalues which satisfy

$$2\tilde{\beta}\sigma^2+[2\mathrm{i}\tilde{\alpha}-\tilde{\beta}(1+2\tilde{\alpha}-\mathrm{e}^{-2\tilde{\alpha}})]\sigma+(\mathrm{i}\tilde{\alpha}-\tilde{\beta})(1-2\tilde{\alpha}-\mathrm{e}^{-2\tilde{\alpha}})=0, \tag{5.12}$$

where $\tilde{\alpha}=\alpha_1 h$, $\tilde{\beta}=\beta U$ and $\sigma=c\tilde{\alpha}/U$, are the dimensionless wavenumber, porosity and eigenvalue. The real phase velocity and the growth rate are given by $c_r/U=\tilde{\alpha}\,\mathrm{Re}(\sigma)$ and $\alpha c_i=U\,\mathrm{Im}(\sigma)/h$.

In the impermeable case, $\tilde{\beta}=0$, only one root survives, which is neutral. Its phase velocity is equal to

$$c_r/U=(\mathrm{e}^{-2\tilde{\alpha}}+2\tilde{\alpha}-1)/2\tilde{\alpha}. \tag{5.13}$$

For very long waves $c_r/U\approx\tilde{\alpha}\ll 1$, and the eigenfunctions fill most of the boundary layer. For short waves, $\tilde{\alpha}\gg 1$, the phase velocity is $c_r\approx U$, and the eigenfunctions are localized in the neighbourhood of the corner of the profile. This neutral shear wave exists for all boundary layer profiles in the inviscid limit. Viscosity damps it, but it remains capable of coupling with the porous boundary condition.

For $\tilde{\beta}\ll\tilde{\alpha}$ we can expand the roots of (5.12) as a series in the porosity coefficient. There are two roots. One of them is proportional to $\tilde{\beta}^{-1}$ and is strongly damped, but the one corresponding to (5.13) becomes unstable. The growth rate is maximum, $\mathrm{Im}(\sigma)\approx 0.14\tilde{\beta}$, at $\tilde{\alpha}\approx 0.387$, and vanishes when $\tilde{\alpha}=0$ or $\tilde{\alpha}\to\infty$. The real part of the phase velocity is unchanged to $O(\tilde{\beta})$.

In the limit of very large porosities, $\tilde{\beta}\to\infty$, all the wavenumbers below $\tilde{\alpha}\approx 1.83$ are unstable. The fastest growth rate tends to $\mathrm{Im}(\sigma)\approx 0.25$, at $\tilde{\alpha}\approx 1.23$. For porosities

between these two extremes all the wavenumbers are unstable, but the growth rates are small for wavenumbers outside the instability range of the infinite porosity case.

There are simple interpretations for the behaviour of the two porosity limits. When $\tilde{\beta} \gg 1$ the porous boundary condition (2.1) is equivalent to $\hat{p}(0) = 0$ which, using (5.5), reduces to $\partial_y \hat{v}(0) = 0$. If we extend antisymmetrically the profile (5.11) to $y < 0$, it becomes a piecewise-linear free shear layer. The condition at $y = 0$ fixes the parity of the solution. The $\hat{v}$ of the infinite-porosity eigenfunctions is even with respect to $y = 0$, inducing sinuous deformations of the shear layer. These are the well-known Kelvin–Helmholtz unstable waves, and they are the only instabilities of this profile (Drazin & Reid 1981, p. 146). The varicose deformations generated by the impermeable boundary condition, $\hat{v}(0) = 0$, are stable. The intermediate porosities connect the Kelvin–Helmholtz instability of the fully permeable wall to the varicose neutral modes of the impermeable one.

A word of caution is needed here. The previous inviscid analysis can be repeated for a channel. There are in that case two neutral modes in the impermeable limit: a varicose one in which $\hat{v}$ is symmetric with respect to the centreline, and a sinuous one in which it is antisymmetric. For short waves both modes are equivalent, and both are approximately equal to the one in the boundary layer. For long waves only the varicose mode resembles that in the boundary layer.

Both modes become unstable when the walls are made porous. For short waves, both are again similar to each other. For long ones, while the varicose mode behaves as in the boundary layer, the sinuous one remains unstable when $\tilde{\alpha} = 0$, and becomes dominant.

Boundary layers are outside the scope of this paper, and the present analysis can only be taken as indicative, but it should be kept in mind that some of the very long modes found in the direct simulations and in the stability analysis of channels, may only be relevant for internal flows.

5.2. *Viscous modes*

The extension of the previous analysis to realistic velocity and eddy viscosity profiles is done numerically. We use a code in which the system (5.3)–(5.5) is discretized by a Galerkin-tau method, using sixth-order B-splines as the expansion functions. The boundary conditions are eliminated by partial Gauss elimination before performing the eigensystem analysis, and all the eigenvalues are computed, with the most unstable one being determined *a-posteriori*. Spurious numerical eigenvalues are eliminated by varying the grid resolution and discarding rapidly changing roots. The procedure was validated against the results of Orszag (1971) and Thomas (1953) for plane Poiseuille flow, and a resolution of 200 splines with an eleven-fold hyperbolic-tangent grid stretching was found satisfactory. We have used it for a channel at the same Reynolds number as our full simulations, in which only the bottom wall is made porous. The eddy viscosity is determined using (5.1) with the mean profile of Reynolds & Tiedermann (1967), with constants adjusted to fit as closely as possible the mean velocity of case I1. It was checked independently that the eigenvalues are not very sensitive to minor details of the velocity profile.

The results are shown in figure 10, as a function of the porosity coefficient and of the wavelength $\lambda_x = 2\pi/\alpha_1$. Very low porosities are now stable, as well as very short and very long waves, but there is a large instability region which contains the two porous cases discussed above. The phase velocities are relatively low for short waves, in which the critical layer is close to the wall, and increase to values comparable to the centreline velocity for long ones, whose eigenfunctions peak farther away. The

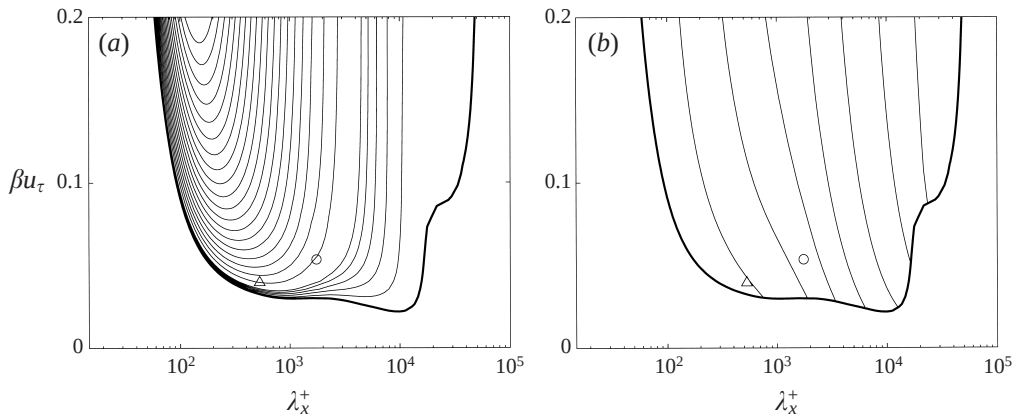

FIGURE 10. Stability characteristic of the turbulent velocity profile in a channel with one porous wall. $Re_\tau = 180$. (*a*) Growth rate of the unstable waves, $\alpha_1 \mathrm{Im}\,(c)\,h/u_\tau = 0(0.1)0.5$ and $1(0.5)10$. (*b*) Phase velocity, $\mathrm{Re}\,(c)/u_\tau = 8(2)20$, increasing from left to right. The heavier solid line is in both cases the neutral border. △, case P1; ○, case P2.

doubling times for the porosities considered in this paper are of the order of the large-scale turnover time, $O(h/u_\tau)$. For very large porosities the eigenvalues approach the Kelvin–Helmholtz limit, as in the inviscid case.

Because of the mean-field assumptions used in the derivation of the instability equations, only those results which refer to wavelengths which are everywhere much longer than the integral scale of the turbulence should be considered quantitative. Perhaps for this reason, the wavelengths observed in the numerical simulations tend to be longer than the most unstable one, which is $\lambda_x^+ \approx 500$ for low porosities. In principle, of course, all unstable wavelengths may be observable in systems in statistical equilibrium, and the selection mechanism is not necessarily linear. The quantitative agreement of other variables is also moderate. The phase velocity for the unstable waves of case P1 is given in figure 10 as $c \approx 8$, but it was measured in figure 8 to be closer to $c \approx 12$. The absolute value of the linear eigenfunctions can be compared with the distribution of two-dimensional energy near the porous wall. Although both agree in having their maxima very near the wall, the peak of the eigenfunction is substantially narrower than that of the measured energy.

6. Transient behaviour

Up to now we have described fully developed flows over a porous surface. Since one of the motivations of this work is the control of boundary layers, it is also important to estimate the length of the transient when porosity is turned on or off. This models the behaviour of a boundary layer flowing over a porous strip, and addresses the question of how wide would the strip have to be to produce a reasonable effect, and how long this effect lasts after the strip ends.

We discuss in this section two experiments, both of which are numerically identical to case I1. In the first one, which is labelled P3 in table 1, the impermeable lower wall of the regular channel I1 is suddenly made porous as in P2. In the second one, labelled I2, the porosity of P2 is suddenly turned off to return to I1. In both cases the moment at which porosity is changed is labelled in the figures as $t = 0$.

The evolution of the friction coefficient is given in figure 11 for both cases. In the

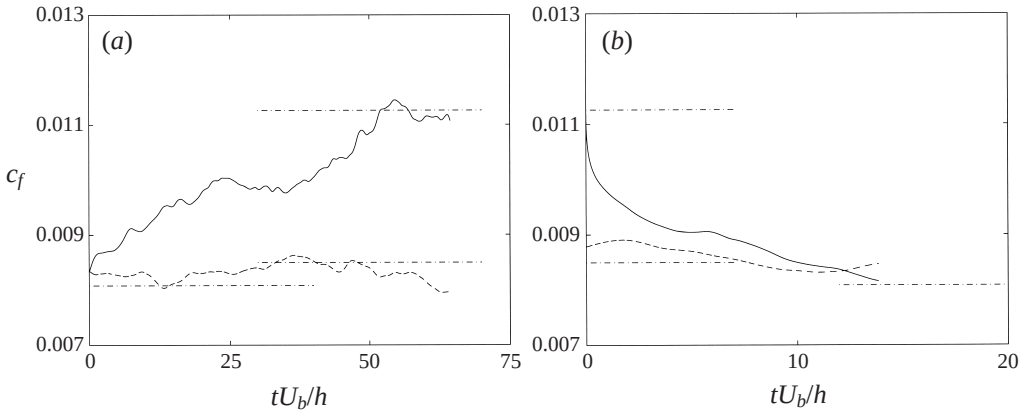

FIGURE 11. Evolution of the plane-averaged wall-friction coefficient after switching porosity between cases I1 and P2: ———, porous wall; – – – –, impermeable wall; —·—, friction coefficients of both walls in the impermeable channel I1, and in the porous one P2. (*a*) Start-up from I1 to P2. (*b*) Decay from P2 to I1.

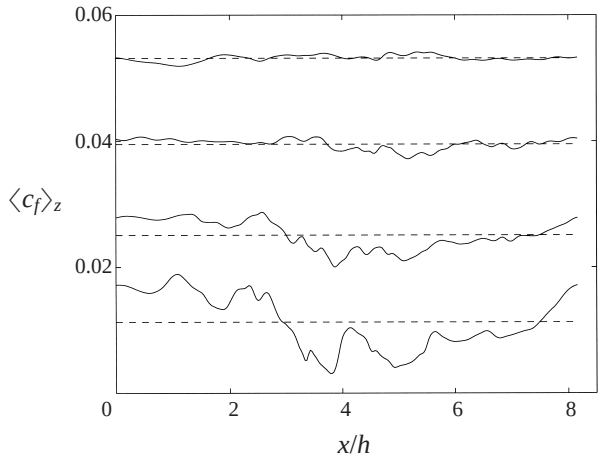

FIGURE 12. Decay of the streamwise modulation of the local friction coefficient in the shut-down case I2. Time grows from bottom to top, $U_b t/h = 0$, 0.4, 1.85, 13.3. Lines are offset for clarity, and the dashed lines are the instantaneous plane-averaged c_f.

start-up case the final equilibrium is reached at approximately $U_b t/h = 60$, which is roughly $u_\tau^2 t/\nu = 700$. The growth of the friction coefficient starts immediately after the porosity is turned on, and increases roughly linearly until reaching its final value. The decay of the friction in the shutdown experiment is faster, and the porous wall returns to the friction levels of the impermeable one at $U_b t/h \approx 10$.

The fast decay of the friction in this latter experiment is accompanied by the disappearance of the streamwise modulation of the friction coefficient, suggesting a rapid decay of the spanwise rollers. This is seen in figure 12 through the evolution of the spanwise-averaged c_f during the shutdown. For the initial porous wall the friction coefficient shows excursions of $\pm 50\%$ along x, but they are quickly damped and, at $U_b t/h \approx 2$, the skin friction is already approximately uniform. At this time the difference between the plane-averaged friction coefficients of the two walls has decreased from being about 30% to less than 10%.

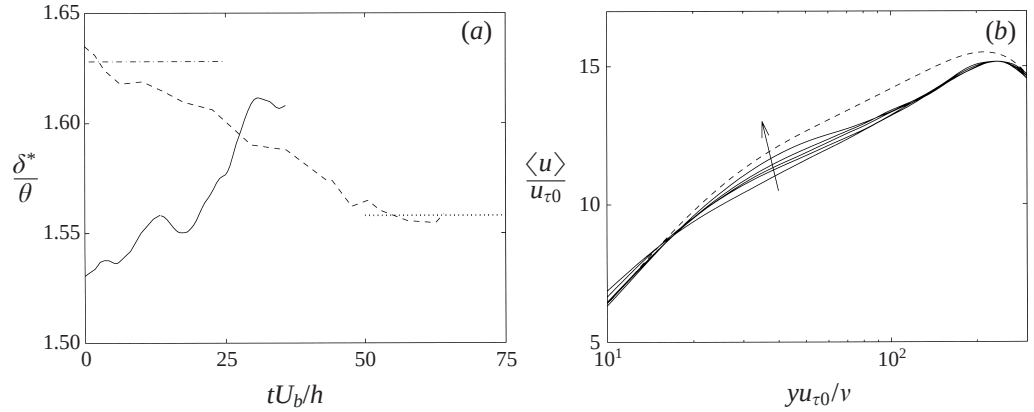

FIGURE 13. (*a*) Variation of the form factor of the boundary layer over the porous wall during the transition: ———, shutdown case I2; – – – –, start-up case P3; —·—, mean form factor for case I1; ·····, mean form factor for case P2. (*b*) Time variation of the instantaneous mean velocity profile for case I2, normalized in the wall units of the porous wall at the beginning of the shut-down. Times are $U_b t/h = 0$, 3.5, 6.4, 10, 13.3, increasing in the direction of the arrow. – – – –, Asymptotic profile of case I1, in the same normalization.

The picture that the rolls, and therefore the effect of porosity, decrease quickly after switching the boundary condition is challenged by figure 13(*a*), which shows the evolution of the form factor of the boundary layer in the bottom part of the channel. This is defined as δ^*/θ where δ^* and θ are the displacement and momentum thicknesses, computed by integrating the instantaneous plane-averaged velocity profiles from the lower wall to the point of maximum velocity. It is a more important quantity technologically than the friction coefficient. If the form factor is low the velocity profile is steep near the wall, and the boundary layer tends to be resilient to separation, while the opposite is true if the form factor is high. The main beneficial effect of locally increasing the friction coefficient in a boundary layer is to decrease its form factor. It is seen in figure 13(*a*) that the form factor of the porous wall is indeed lower than that of the impermeable one but that, unlike the evolution of the friction coefficient, the time that it needs to adapt to the change of the boundary condition is comparable during the start-up and during the shutdown, and is in both cases long. This suggests that the fast decay of the friction in the shutdown is a local effect in the neighbourhood of the wall, which only affects slowly the boundary layer as a whole.

This is confirmed by figure 13(*b*), which shows the instantaneous plane-averaged velocity profiles during the initial part of the shutdown. The profile very close to the wall changes quickly, but the outer part is not changed, and the resulting bulge grows only slowly to change the profile to its impermeable shape.

In figure 14 we have mapped the outwards diffusion of the effect of the boundary condition in both cases. We have used the evolution of the spanwise correlation length,

$$L_{uu,z} = \int_0^{L_z} R_{u'u'}(z)\,\mathrm{d}z, \tag{6.1}$$

which gives an idea of the growth of the two-dimensional mode. We see in figure 14(*a*) that this length is uniformly small in the impermeable channel, at $t = 0$, and begins to grow very near the wall immediately after the porosity is switched on. After a delay of about $U_b t/h \approx 25$ during which the two-dimensionality stays confined below $y^+ = 20$, there is a more or less linear diffusion away from the wall. In this

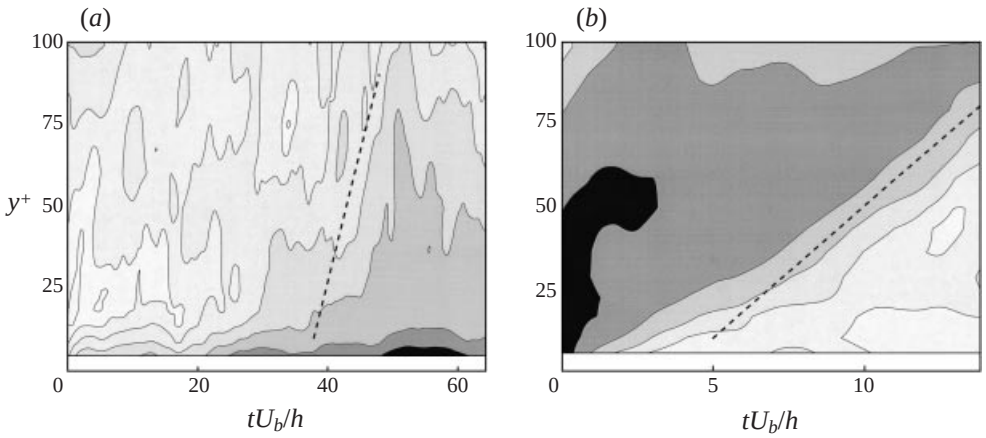

FIGURE 14. Evolution of wall-normal distribution of the spanwise correlation length $L_{uu,z}$. Contours are $L^+_{uu,z} = 0.5(\times 2)32$, going from light to dark. (*a*) Start-up case P3. (*b*) Shutdown case I2. The dotted lines in both plots have slope $\mathrm{d}y^+/\mathrm{d}t^+ \approx 0.6$.

particular case this happens in two episodes, one around $U_b t/h \approx 30$ and the other at $U_b t/h \approx 45$. By the time the second burst reaches $y^+ \approx 40$ the friction coefficient is near its asymptotic value, and the flow is essentially at equilibrium. The behaviour during shutdown is different in that the initial transient is missing. The near-wall structures are destroyed immediately after the porosity is switched off, and the linear diffusion away from the wall starts without delay. This vertical diffusion happens at about the same rate in both cases. The dotted lines in the two contour maps have a slope $\mathrm{d}y^+/\mathrm{d}t^+ \approx 0.6$.

If we interpret the growth and decay of the form factor as due to the formation and destruction of the spanwise rollers, which we found in the previous section to move at $U \approx 12u_\tau$, the characteristic start-up time, $\Delta t^+ = 700$, would correspond to a distance of about $\Delta x^+ = 8000$, or about 40 boundary layer thicknesses.

The observations in this section can be compared to those of He & Jackson (2000) on the evolution in turbulent pipes subject to a sudden increase in the flow rate. They also find that turbulence is modified starting from the wall, and identify two stages. In the first one, which lasts about 100 wall units, the effect of the boundary condition diffuses through the viscous sublayer until it reaches the location of the turbulence production peak at $y^+ \approx 10$. This would correspond to the initial delay in figure 14(*a*), and is roughly consistent with our value of $U_b t/h = 25 \approx 250^+$. In a second stage, the turbulence production is modified, and the effect is transmitted outwards at a constant wall-normal velocity of the order of $0.7u_\tau$. This is also not too far from the slope of the dotted lines in figure 14. Since their experiments are done at $Re_\tau \approx 10^3$, which is substantially higher than ours, and the details of their forcing are also quite different, this rough agreement suggests that our results on the length of the transients should scale to situations of practical interest as multiples of the boundary layer thickness.

7. Active control

We have discussed up to now a passive control configuration, in which the natural instability of the flow is used to generate coherent structures, which in turn modify

Case	U_c^+	v_{rms}^+	c_{fb}/c_{f0}	c_{fb}/c_{ft}
F1	0	0.06	1.09	1.00
F2	10	0.1	1.11	1.06
F3	10	0.2	1.27	1.21
F4	0	0.2	1.15	1.04
F5	2	0.2	1.15	1.10
F6	5	0.2	1.58	1.40
F7	8	0.2	1.56	1.36
F9	12	0.2	1.12	1.06
F10	15	0.2	1.10	1.01

TABLE 3. Active control experiments. U_c^+ is the phase velocity of the forced harmonic transpiration, and v_{rms} is its r.m.s. intensity. Both are normalized with the friction velocity of the unforced impermeable channel. c_{fb} and c_{ft} are the friction coefficients on the porous and impermeable walls, and they are compared with the value c_{f0} of the reference case I1. In all cases the forcing wavelength was equal to the box length, $\lambda_x = 2.69h \approx 490^+$.

the flow and the skin friction. We have mentioned some problems with this approach. In the first place, the only control parameter is the porosity, which may be hard to manipulate dynamically. We also noted in the introduction that it might be difficult to avoid large-scale recirculation through the plenum chamber in the presence of macroscopic pressure gradients, and we later found, in figure 14(*a*), that the development time of the instability is not a negligible fraction of the time needed by porosity to modify the flow.

All these problems suggest the convenience of developing active control strategies involving distributions of local transpiration which are independent of the pressure fluctuations at the wall. Those patterns could presumably be generated using MEMS, and therefore be available 'on demand', and they would bypass the slow growth of the porous instability. Moreover, since it follows from the arguments in the previous sections that the main effect of porosity is to initiate the spanwise rollers, it should be possible to implement such strategies in 'open loop', forcing rolls of the right wavelength and phase velocity without locally sensing the microscopic flow variables. A final advantage of the numerical experiments needed to test such active controls is that they allow us to study in detail the effect of the rollers on the flow by means of phase averaging.

Those experiments are discussed in this section. A spanwise-coherent wall transpiration is imposed on the wall, with the form

$$v = \sqrt{2} v_{rms} \sin\left[k_x(x - U_c t)\right]. \tag{7.1}$$

Its aim is to take advantage of the natural instability of the flow to generate the largest possible change in the friction coefficient with a given wall transpiration. The experiments are listed in table 3, and the resulting changes in the friction coefficient are collected in figure 15(*a*), which also includes the porous cases. There are two sets of experiments. In the first one the phase speed of the forcing is kept constant, $U_c^+ = 10$, and the transpiration amplitude is changed, while in the other the amplitude is kept constant and the phase velocity is changed. All the experiments are done in the smaller of the two numerical boxes given in table 1, to allow a reasonably complete parameter scan within the available computer time. As discussed in the introduction this box is large enough to contain most of the structures in regular channels but, as in the case of porosity, the forcing wavelength, which is always the length of the box,

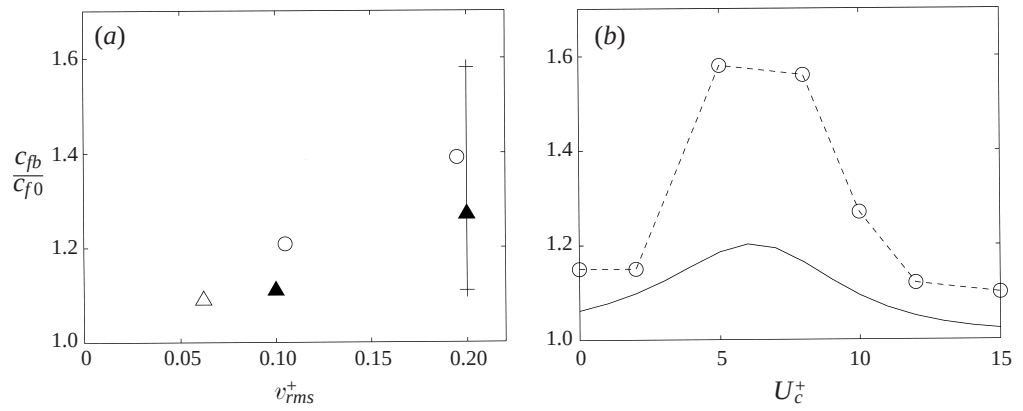

FIGURE 15. (*a*) Friction coefficients of the forced and porous experiments, in terms of the transpiration intensity: ○, porous cases; △, forced, $U_c = 0$; ▲, forced, $U_c^+ = 10$. The vertical bar is the range obtained at this intensity with different phase velocities. (*b*) ○, Friction coefficients as a function of the phase velocity. $v^+_{rms} = 0.2$. The dashed line is drawn to aid the eye. ———, Friction coefficient predicted from the linear analysis (5.9). The wall units are those of the impermeable channel. In all cases the forcing wavelength was equal to the box length, $\lambda_x = 2.69h \approx 490^+$.

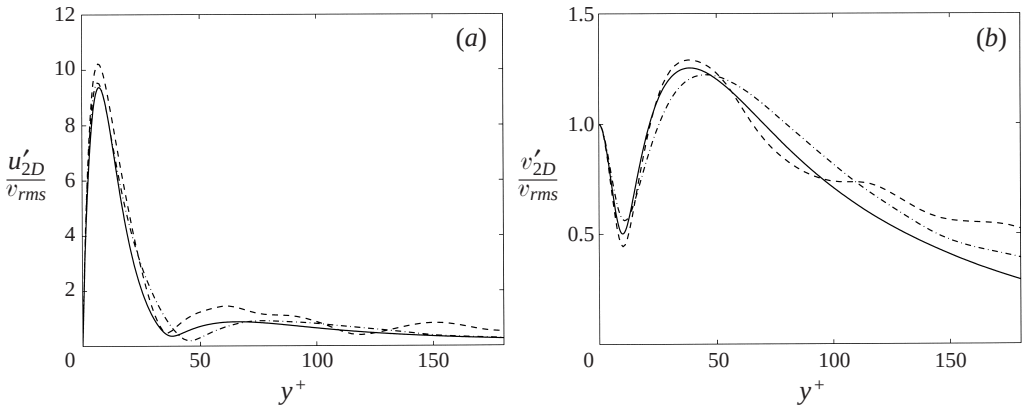

FIGURE 16. Profiles of the spanwise-coherent fluctuation intensities, normalized with the forcing v_{rms}. The phase velocity is $U_c^+ = 10$. ————, $v^+_{rms} = 0.1$; —·—, $v^+_{rms} = 0.2$; ———, linear calculation. (*a*) $\langle \bar{u}^2 \rangle_t^{1/2}$, (*b*) $\langle \bar{v}^2 \rangle_t^{1/2}$.

is too short to be optimal. The numerical resolution is given in table 1 for the case F2, and is similar for all the other cases. It is comparable to, or better than, the ones used in the porous simulations and in the channel of Kim *et al.* (1987). A simulation similar to case F6, with the same short forcing wavelength, was run in the larger box of case I1 to test for possible gross artifacts due to the box size, but none was found.

The first series of experiments was used to estimate the maximum practical forcing amplitude. Above $v^+_{rms} \approx 0.2$, local separation appears, in agreements with the limits found for porous walls. The high-amplitude forcing experiments which resulted in separation were not continued for long times, and are not reflected in table 3.

The second series of tests was designed to check whether what was being forced was the instability studied in § 5, by looking for a resonance peak in terms of the convection velocity. The friction coefficients of those cases are given in figure 15(*b*).

There is indeed a broad peak, which is not too far from the convection velocity given in figure 10 for the unstable rolls at this wavenumber.

A more direct test of the linear analysis is to compare the forced nonlinear results with the forced solutions of the Orr–Sommerfeld equation (5.3). Those can be obtained by using $\hat{v}(0) = 1$ at the lower wall, instead of the porosity condition, while substituting an arbitrary phase velocity U_c for the eigenvalue c.

The relevant linear modes in this case are not those of the porous channel, but the least damped ones of an impermeable one. If we return for a moment to the inviscid linear analysis in § 5.1, those are the neutral modes of the inviscid profile. If the system were driven in that case by a sinusoidal transpiration velocity moving with a phase velocity U_c, the response would be the superposition of an inhomogeneous term, which decays exponentially away from the wall, and a resonant component proportional to the eigenfunction of that particular wavenumber. The amplitude of this second component would be proportional to $1/(U_c - c)$, where c is the eigenvelocity. In the inviscid case it would become infinite when the two velocities coincide. Viscosity, or in turbulent flows eddy viscosity, damps these modes and makes the resonance peak broader and of finite amplitude. That the linear analysis explains most of the spanwise coherent fluctuations is seen in figure 16, which compares the two-dimensional intensities for two flows forced at different amplitudes, but with the same wavenumbers and phase velocities, with the result of the linear calculations. Each curve is normalized with its own transpiration r.m.s. velocity, and not only is the linear scaling satisfied well, but the agreement with the linear analysis is excellent.

We have included in figure 15(*b*) the linear prediction for the change in the friction coefficient, based on the analysis in § 5.1. This is the change in friction due to the Reynolds stresses of the two-dimensional fluctuations plotted in figure 16. The position of the peak is predicted well, supporting the conclusion that the mechanism involved is indeed a resonance, but its amplitude is too low by a factor of about three. This agrees with the conclusions of the discussion of (5.9), which was that the two-dimensional structures are the seed, but not the only contributors, to the enhanced turbulent activity.

That the rollers are being generated by the forcing is shown in figure 17, which contains flow fields averaged with respect to the phase of the forcing. The isolines in both parts of the figure correspond to the spanwise-averaged velocity in the frame of reference moving with the forcing wave. They show the cat's-eye pattern of the rollers, which are centred near the linear critical layer at which $\langle u \rangle = U_c$. Figure 17(*a*) includes a map of the local intensity of the incoherent fluctuations u'', which are defined with respect to the local phase-averaged velocity by (3.7). It shows how the rollers modulate the turbulent quantities and, in particular, how the fluctuations are intensified by the artificial 'ejection' at the trailing edge of the rollers, while being damped by the 'sweep' which follows it.

Figure 17(*b*) shows the spanwise-averaged ω_z, which is the vorticity component responsible for the wall friction. It is clear that most of the extra skin friction is generated where the flow is forced by the rollers into the wall.

Finally, in figure 18(*a*) we show the change of the friction coefficient predicted by the linear stability analysis, as a function of the wavelength and of the phase velocity of the forcing. The dashed line is the eigenvalue of (5.3), and agrees well with the ridge of maxima of the forced response, supporting again the idea of a resonance. The eigenvalue used in this figure was computed by numerical continuation from the only eigenvalue whose phase velocity at short wavelengths is clearly slower than the phase velocity. Its energy is initially contained near the wall but, as the wavelength increases,

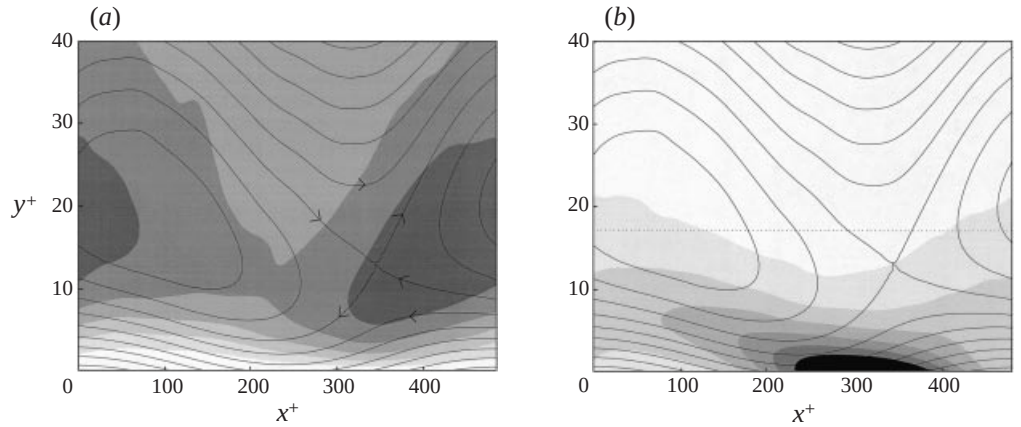

FIGURE 17. Phase-averaged flow fields from the forced case with $v^+_{rms} = 0.2$ and $U^+_c = 10$. In both plots the streamlines are from the spanwise-averaged velocity in a frame of reference moving with the forcing. The flow moves from left to right at the top of the figure, and in the opposite direction near the wall. The flux between neighbouring streamlines is $0.0037U_b h$. (*a*) Incoherent intensity of the streamwise velocity, $\langle u''^2\rangle^{1/2}_{zt}$, stronger from light to dark. The contour increment is $0.5u_\tau$. (*b*) Spanwise-averaged spanwise vorticity, stronger from light to dark. The contour increment is $0.25u^2_\tau/\nu$. The dotted line is the linear critical layer $\langle u\rangle = U_c$.

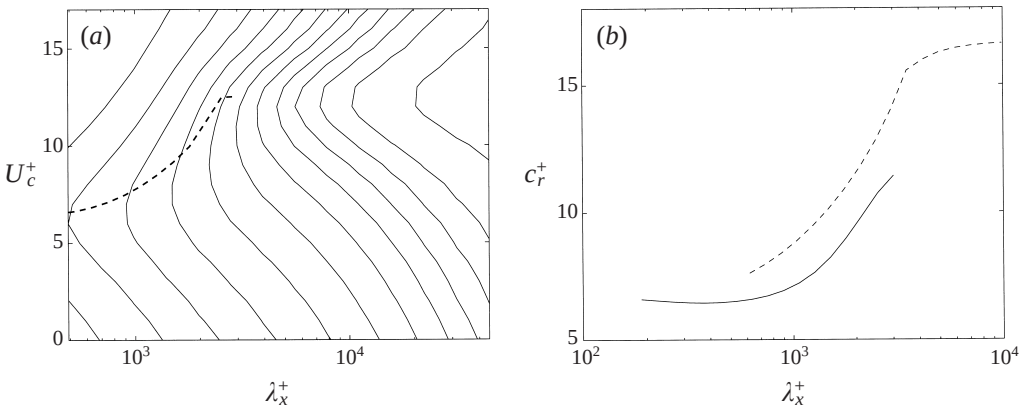

FIGURE 18. (*a*) Response to forcing, measured by the predicted increase in friction coefficient, as a function of the wavelength and the phase velocity. The solid contours are $\Delta c_{fb}/(c_{f0}v^2_{rms}) = 3(3)36$, increasing from left to right; – – – –, real part of the eigenvalues from the linear stability problem. $Re_\tau = 180$. (*b*) Real part of the stability eigenvalues. ———, $Re_\tau = 180$; – – – –, $Re_\tau = 590$.

the eigenfunction moves away from the wall and the phase velocity increases. All the other eigenvalues have real parts which are comparable with the centreline velocity, and eigenfunctions which reside away from the wall at all wavelengths. In figure 18(*b*) we plot the real part of the eigenvalue compared with results at $Re_\tau = 590$. They agree with each other in wall units better than in outer units, suggesting that this would also be the case for the real response of forced turbulent channels. The damping times of these eigenvalues are in both cases of the order of 10–$20\nu/u^2_\tau$. They are therefore close to neutral from the point of view of turbulence.

The predicted amplitude of the forced response increases with increasing wavelengths, essentially because a deeper layer participates in the eigenfunction, but the

effect levels off at very long wavelengths for which the profile accelerates and decelerates as a unit. This would be the preferred range of operation for a practical application of forcing to increase the skin friction, but it should be interpreted with care when applied to external flows, in the light of the discussion at the end of § 5.1.

8. Discussion and conclusions

We have shown that passive porous walls increase skin friction by substantial amounts, which are limited to about 40% by the appearance of local flow separation. We have shown that this effect is unrelated to the roughness effect of discrete pores, since our porosity is smoothly distributed. The extra drag is in part due to the energy dissipated as the transpiration crosses the permeable wall, but this loss only explains about 10% of the total drag increase. The rest is due to a large-scale reorganization of the flow, over distances comparable with the channel half-width, which originates from a linear instability resulting in coherent spanwise rolls. The rolls increase drag by creating large-scale 'sweeps' in which the velocity is directed into the wall, locally increasing the skin friction, and 'ejections' in which the instability and intensity of the velocity streaks is enhanced.

We have connected the linear instability responsible for the rolls to the neutral shear waves of the inviscid mean velocity profile. Although these modes are damped by viscosity in real channels, they couple to the porosity condition and become unstable, even when the porosity coefficient is small. The root-mean-square transpiration velocities measured in the porous simulations are of the order of $0.1u_\tau$. It is also these modes which are excited in our forced simulations, as shown by the resonance effect when the advection velocity of the forcing agrees with the phase velocity of the almost-neutral eigenfunctions of the velocity profile. When the rolls are excited in this way the skin friction also increases, to levels which are even higher than those achieved with passive porosity. The forced experiments have been used to confirm, by means of phase-locked averaging, the mechanisms hypothesized to explain the effect of porosity.

Our investigation was motivated by the possibility of using either passive porosity or active transpiration as 'on demand' roughness to delay separation in boundary layers. The study of resonant active forcing was originally undertaken to remedy some difficulties identified in the practical use of passive porous surfaces. Although implementation issues are not part of this paper, it is interesting to note that the control strategies based on this effect would be both large scale and open loop. There have been many attempts to control drag by manipulating the stability of individual streaks, some of which are mentioned in the introduction. While this has been demonstrated in some cases, those strategies are generally both small scale, with actuators which must have dimensions of a few wall units, and closed loop, requiring local flow sensing. The wall unit in air at high subsonic speeds is of the order of 1 μm, placing strong constraints on the implementation of sensors and actuators. Although our simulations are limited to a single Reynolds number, we have estimated scaling laws whenever possible by comparing with related experiments. We have found for example that the length needed to switch the effect of porosity on and off probably scales with the boundary layer thickness. Although not discussed in detail here, a comparison of the linear stability results at two different Reynolds numbers suggests that the most effective forcing wavelength is of the order of several boundary layer thicknesses. We have however mentioned that this last conclusion should be applied with care to external flows, in view of the differences observed in the simplified linear analysis of boundary layers and channels.

In any case, the forcing of the flow can be implemented without reference to the instantaneous flow variables, except for large-scale information on the state of the boundary layer, since the control parameters are the known wavelength and advection velocity of the forcing.

Although we mentioned in the introduction several experiments in which passive porosity has been shown to increase drag by amounts comparable to those found in this paper, there are to our knowledge no experiments on the effects of periodic travelling transpiration waves. The closest are perhaps on the delay of separation by the periodic addition of momentum at the root of a hinged flap, reviewed by Wygnanski (1997). He forces the boundary layer with a pulsating massless two-dimensional jet near the hinge, and finds that there are two effects with different characteristic parameters. The reattachment on a stalled flap is due to the enhancement of the entrainment of the separated free shear layer, bleeding fluid from the recirculating bubble, and is presumably different from the effect of periodic forcing observed in our case. The maintenance of the attached boundary layer, on the other hand, should be closer to our problem. He finds that the forcing frequency that is most efficient in preventing separation is $4L_f/U_\infty$, where the choice of the flap length L_f as a characteristic length is geometry-dependent and is justified in Seifert *et al.* (1993). Since the measured advection velocity of the resulting pressure fluctuations is about $0.45U_\infty$ and the displacement thickness of the resulting boundary layer is of the order of $\delta^*/L_f = 0.04$, this corresponds to a wavelength of about $3\delta^*$. Since in a channel $\delta^*/h \approx 0.14$, this would put his optimum forcing in the range of very short waves, for which such a low convection velocity is reasonable. The very different geometries of the two cases, and especially the qualitative differences between the velocity profiles of a fully attached channel and of a flap near separation, make any further quantitative comparison impossible.

There are several outstanding issues which need clarification before this problem can be considered closed. Although the agreement between the the forced spanwise-averaged fluctuations and the linear analysis has been shown to be excellent, we have mentioned that the measured spanwise rollers over passive porous walls extend deeper into the flow than the two-dimensional linear eigenfunctions, and that, both in the forced and in the passive cases, the observed change in the skin friction is two or three times larger than the one predicted from two-dimensional linear analysis. We have of course no right to expect strict linear behaviour of a flow in which the skin friction increases by 50%, but these discrepancies are bothersome and should eventually be clarified.

A fascinating possibility, which has also not been pursued here but which is under active investigation in our group, is that the quasi-neutral linear eigenfunctions identified in this paper may be related to the very large scales observed in wall flows (Jiménez 1998; Kim & Adrian 1999). They have comparable wavelengths and reside at similar locations within the boundary layer and, although they are made unstable here by their coupling to the porosity condition, it is easy to imagine interaction mechanisms with the near-wall layer that would also make them unstable in an impermeable channel. The low value of the wall-normal velocity needed to get a large effect in the porous case suggests that relatively weak interactions might be sufficient.

Finally, experimental confirmation of both the flow structure and the effects of the forcing is clearly desirable.

This work was supported in part by the Brite EuroMems program, managed by British Aerospace and by Dassault Aviation, by the Spanish CICYT contract

PB95-0159 and by ONR grant N0014-00-1-0146. A.P. was supported in part by an independent grant from CICYT and G.K. by the Japanese Ministry of Education, Science and Culture. The application of local drag enhancement to separation control was originally suggested by P. Perrier.

REFERENCES

Addington, G. A., Schreck, S. J. & Luttges, M. V. 1992 Static and dynamic flow field development about a porous suction surface wing. *AIAA Paper* 92-2628.

Batchelor, G. 1967 *An Introduction to Fluid Dynamics*. Cambridge University Press.

Carpenter P. W. 1996 The possibility of using passive porous walls for drag reduction. In *Emerging Techniques in Drag Reduction* (ed K.-S. Choi, K. K. Prasad & T. V. Truong), pp. 221–242 Mechanical Engineering Publications.

Choi, H., Moin, P. & Kim, J. 1994 Active turbulence control for drag reduction in wall-bounded flows. *J. Fluid Mech.* **262**, 75–110.

Drazin, P. G. & Reid, W. H. 1981 *Hydrodynamic Stability*. Cambridge University Press.

Gad el Hak, M. & Blackwelder, R. F. 1989 Selective suction for controlling bursting events in a boundary layer. *AIAA J.* **27**, 308–314.

Gillan, M. A. 1995 Computational analysis of buffet alleviation in viscous transonic flow over a porous airfoil. *AIAA J.* **33**, 769–772.

He, S. & Jackson, J. D. 2000 A study of turbulence under conditions of transient flow in a pipe. *J. Fluid Mech.* **408**, 1–38.

Houstis, E. N., Vavalis, E. A. & Rice, J. R. 1988 Convergence of $O(h^4)$ cubic spline collocation methods for elliptic partial differential equations. *SIAM J. Numer. Anal.* **25**, 55–74.

Jiménez, J. 1994 On the structure and control of near wall turbulence. *Phys. Fluids* **6**, 944–953.

Jiménez, J. 1998 The largest scales of turbulent wall flows. *CTR Ann. Res. Briefs, Stanford University*, 137–154.

Jiménez, J. & Moin, P. 1991 The minimal flow unit in near-wall turbulence. *J. Fluid Mech.* **225**, 213–240.

Jiménez, J. & Pinelli, A. 1999 The autonomous cycle of near-wall turbulence. *J. Fluid Mech.* **389**, 335–359.

Jiménez, J., Pinelli, A. & Uhlmann, M. 1998 Plane channel flow simulation over porous walls. *Technical Note* ETSIA MF-9809, School of Aeronautics, Universidad Politécnica Madrid, Spain.†

Kim, J. 1989 On the structure of pressure fluctuations in simulated channel flow. *J. Fluid Mech.* **205**, 421–451.

Kim, J. & Hussain, F. 1993 Propagation velocity of perturbations in turbulent channel flows. *Phys. Fluids* A **5**, 695–706.

Kim, J., Moin, P. & Moser, R. 1987 Turbulence statistics in a fully developed channel flow at low Reynolds number. *J. Fluid Mech.* **177**, 133–166.

Kim, K. C. & Adrian, R. J. 1999 Very large-scale motion in the outer layer. *Phys. Fluids* **11**, 417–422.

Kong, F. Y. & Schetz, J. A. 1982 Turbulent boundary layer over porous surfaces with different geometries. *AIAA Paper* 82-0030.

Löfdahl, L. & Gad-el-Hak, M. 1999 MEMS applications in turbulence and flow control. *Prog. Aerospace Sci.* **35**, 101–203.

Lucas, T. R. 1974 Error bounds for interpolating cubic splines under various end conditions. *SIAM J. Numer. Anal.* **11**, 569–585.

Orlandi, P. & Jiménez, J. 1994 On the generation of turbulent wall friction. *Phys. Fluids* **6**, 634–641.

Orszag, S. 1971 Accurate solution of the Orr–Sommerfeld equation. *J. Fluid Mech.* **50**, 689–703.

Perot, B. & Moin, P. 1995 Shear-free turbulent boundary layers. Part 1. Physical insights into near-wall turbulence. *J. Fluid Mech.* **295**, 199–227.

Reynolds, W. & Tiedermann, W. 1967 Stability of turbulent channel flow, with application to Malkus's theory. *J. Fluid Mech.* **27**, 253–272.

† Available from the JFM Editorial Office, Cambridge, on request.

SCHOPPA, W. & HUSSAIN, F. 1997 Effective drag reduction by large-scale manipulation of streamwise vortices in near-wall turbulence. *AIAA Paper* 97-1794.

SEIFERT, A., BACHAR, T., KOSS, D., SHEPSHELOVICH, M. & WYGNANSKI, I. 1993 Oscillatory blowing, a tool to delay boundary layer separation. *AIAA J.* **31**, 2052–2060.

SUMITANI, Y. & KASAGI, N. 1995 Direct numerical simulation of turbulent transport with uniform wall injection and suction. *AIAA J.* **33**, 1220–1228.

THOMAS, L. 1953 The stability of plane Poiseuille flow. *Phys. Rev.* **91**, 780–791.

WAGNER, C. & FRIEDRICH, R. 1998 On the turbulence structure in solid and permeable pipes. *Intl J. Heat Fluid Flow* **19**, 459–469.

WILKINSON, P. 1983 Influence of wall permeability on turbulent boundary-layer properties. *AIAA Paper* 83-0294.

WYGNANSKI, I. 1997 Boundary layer control by periodic addition of momentum. *AIAA Paper* 97-2117.